SUPPLEMENTARY INFORMATION

Disorder Induced Quantum Griffiths Phase in the Proximate Kitaev Quantum Spin Liquid $Na_2Co_2TeO_6$

Wassilios Papawassiliou[1]*, Nicolas Lazaridis[2,3], Eunice Mumba Mpanga[4], Jonas Koppe[1], Nikolaos Panopoulos[2], Lydia Gkoura[5], Romain Berthelot[4], Michael Fardis[2], Gaël De Paëpe[6], Andrew J. Pell[1,7], and Georgios Papavassiliou[2]*

Affiliations [1] Centre de RMN à Très Hauts Champs de Lyon (UMR 5280 CNRS / ENS Lyon / Université Claude Bernard Lyon 1), Université de Lyon, 5 rue de la Doua, 69100 Villeurbanne, France

[2] Institute of Nanoscience and Nanotechnology, National Center for Scientific Research "Demokritos", 153 10 Aghia Paraskevi, Attiki, Greece

[3]School of Applied Mathematical and Physical Sciences, National Technical University of Athens, 15780 Zografou, Athens, Greece

[4]ICGM, Univ Montpellier, CNRS, ENSCM, Montpellier 34095, France

[5]BRC, Technology Innovation Institute, PO Box 9639, Masdar City, Abu Dhabi, UAE

[6]Université Grenoble Alpes, CEA, IRIG, MEM, Grenoble 38000, France

[7]Institut Universitaire de France (IUF)

*Corresponding authors: wassilios.papawassiliou@ens-lyon.fr, g.papavassiliou@inn.demokritos.gr

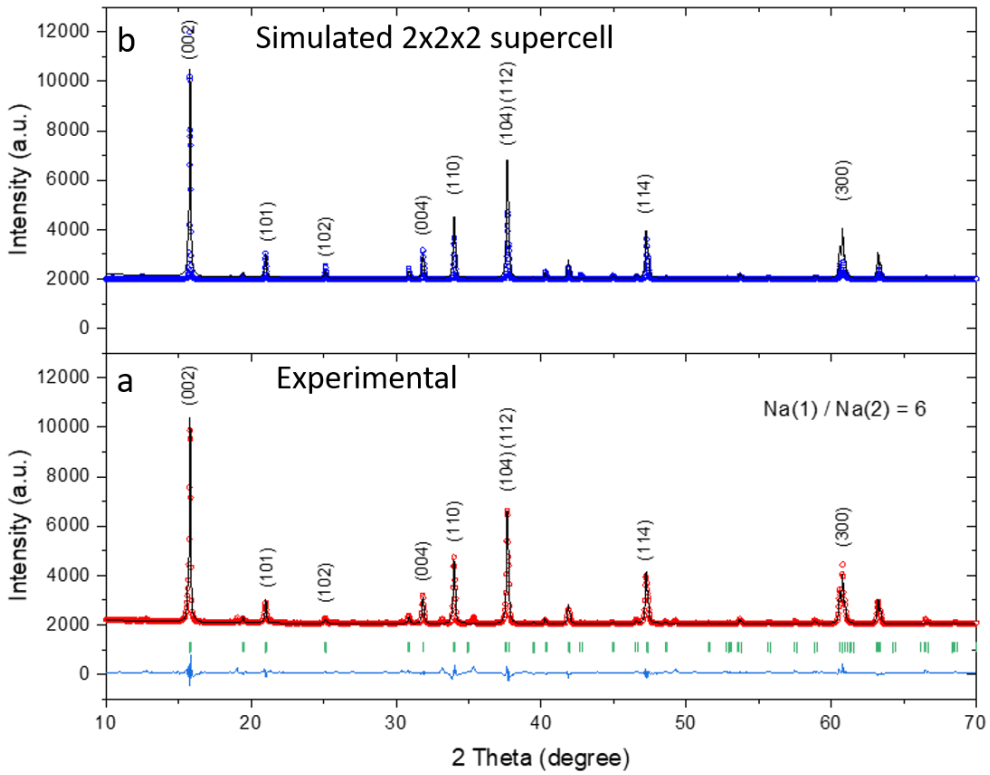

Supplementary Figure S1 | XRD analysis of NCTO. a, Experimental XRD intensities (red circles) and Rietveld analysis (solid line) for NCTO at room temperature, with sodium occupying two distinct

crystallographic positions. Bragg peak positions are indicated by vertical bars, while the difference plot is displayed at the bottom of the panel. **b,** Simulated XRD pattern (blue circles) of the 2x2x2 NCTO supercell with random Na occupancy. Solid line is the Rietveld analysis of the experimental XRD from panel (a).

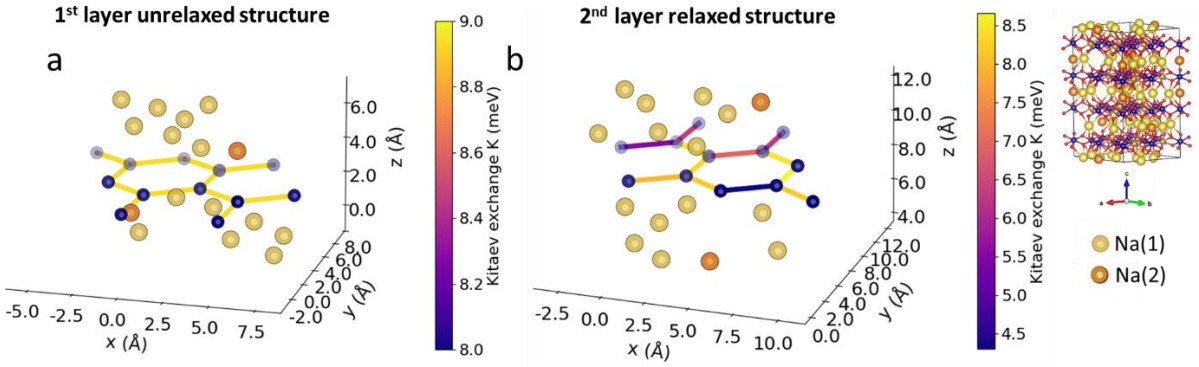

Supplementary Figure S2 | Distribution of the Kitaev exchange couplings *K* across Co-layers in a 2x2x2 NCTO supercell. a, Color-coded map of K across the first Co-layer in the unrelaxed supercell. The values were obtained using the phenomenological expression $K = K_{\max}\,[1 - c(\theta - \theta_0)^2]\,(r_0/r)^p$, with parameters $r_0 \approx 2.11$ Å, $\theta_0 \approx 92°$, according to the XRD Rietveld analysis, $K_{\max} \approx 9$ meV, $p = 10$, and $c = 0.1$. The selection of $p = 10$ is explained in Supplementary Note 3. **b,** Color-coded K-map across the second Co-layer in the DFT-relaxed supercell. The parameters used in this case were $r_0 \approx 2.05$ Å, $\theta_0 \approx 95°$ (median values of the r and θ distributions), $K_{\max} \approx 9$ meV, $p = 10$, and $c = 0.1$.

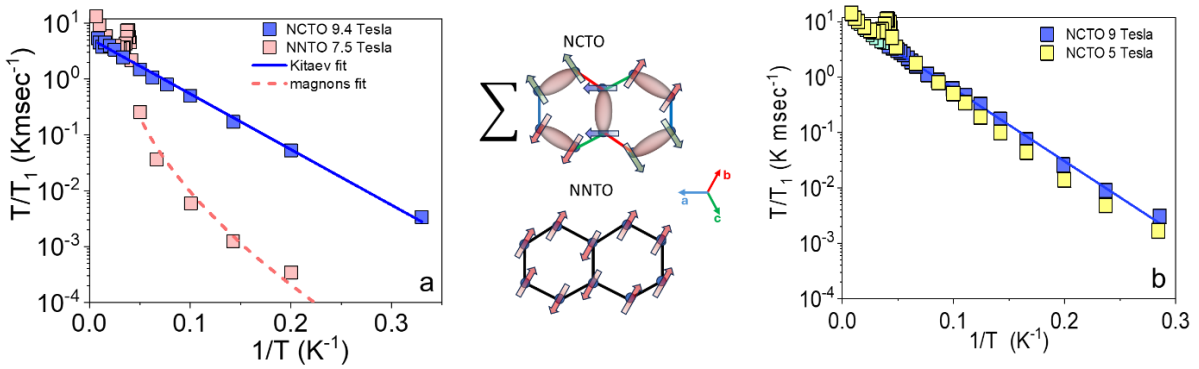

Supplementary Figure S3 | ^{23}Na NMR T/T$_1$ vs. 1/T analysis illustrates dominance of Kitaev fractional excitations in NCTO in a strong magnetic field. a, T/T_1 vs. $1/T$ of the slow relaxing component in NCTO (blue squares) for the entire temperature range under a magnetic field of 9.4 T. Comparison with the corresponding plot for $Na_2Ni_2TeO_6$ (NNTO) in a magnetic field of 7.5 T (red squares, compiled from ref. [35] of the main article). **b,** T/T_1 vs. $1/T$ of NCTO in magnetic fields of 5 Tesla (yellow squares) and 9 Tesla (blue squares), compiled from reference [36] in the main article. The blue solid line represents the fit according to eq. (1) of the main article. The central image shows in the

upper panel: the Kitaev spin configuration (Σ represents the superposition of all entangled Kitaev spin states), anticipated for NCTO, and in the lower panel: the zig-zag antiferromagnetic (AFM) spin configuration in NNTO.

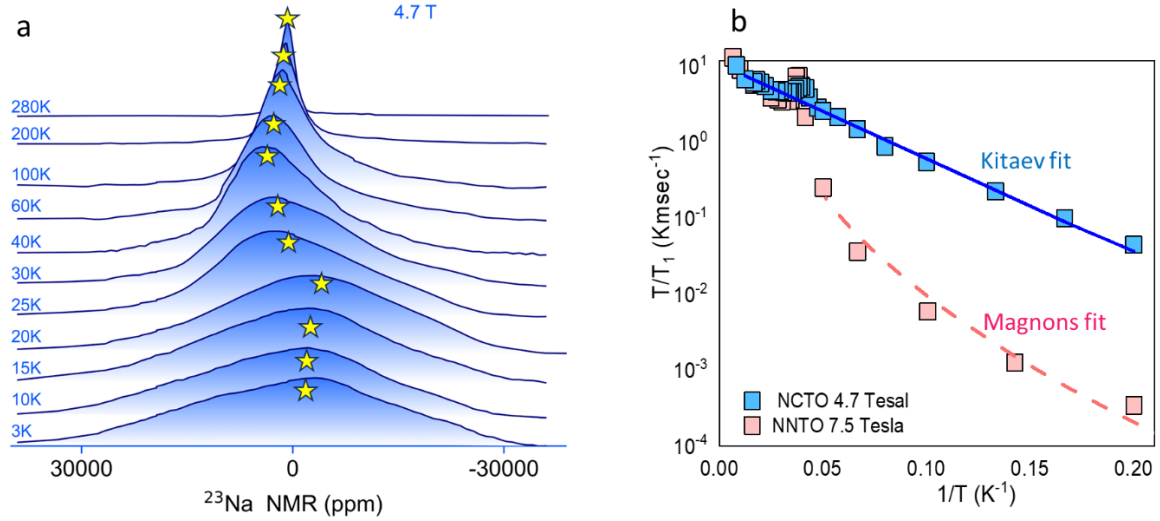

Supplementary Figure S4 | Coexistence of magnon and fractional excitations in NCTO at 4.7 Tesla. a, Temperature evolution of static ^{23}Na NMR spectra from 300 K to 3 K at 4.7 T. **b,** ^{23}Na NMR T/T_1 vs. $1/T$ plots for NCTO (blue squares) at 4.7 T and NNTO at 7.5 T (red squares, obtained from ref. [35] of the main article). Blue and red lines are fits to eq. (1) and eq. (2) of the main article.

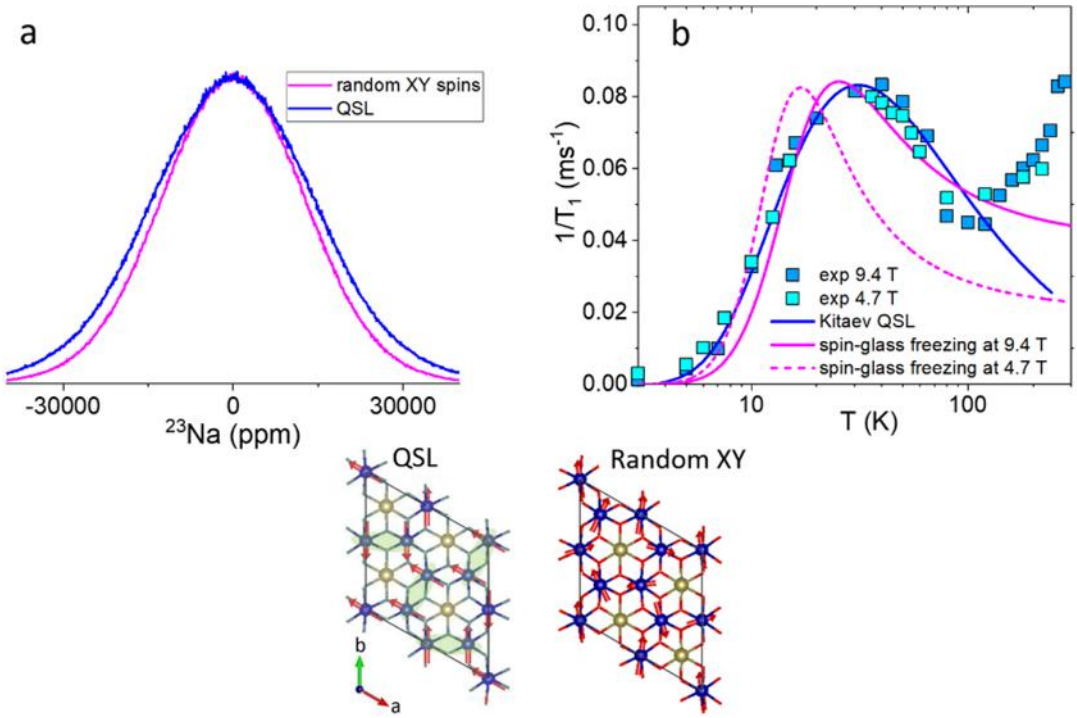

Supplementary Figure S5 | Conventional spin-glass freezing is not validated by ^{23}Na NMR T_1 relaxation measurements. a, *Ab initio* simulated ^{23}Na NMR powder patterns for a Kitaev quantum spin liquid (QSL) and a random in-plane (XY) spin configurations at 9.4 T, overlaid on the DFT-relaxed 2×2×2 supercell. Both configurations yield similarly broadened lineshapes, indicating that static

spectral broadening alone cannot distinguish between QSL and spin-glass-like textures. **b,** Temperature dependence of the spin-lattice relaxation rate, $1/T_1$, for NCTO at 4.7 T (cyan squares) and 9.4 T (blue squares). The two datasets exhibit nearly identical temperature dependences, with a striking overlap at low temperatures. For clarity, the 4.7 T data near the PM-AFM transition ($T_N \approx 27$ K) and the fast-relaxing component, at both magnetic fields, below 10 K are omitted. The purple curves show simulations using a Bloembergen-Purcell-Pound (BPP) model at 9.4 T (solid line) and 4.7 T (dashed line), combined with a Vogel-Fulcher temperature dependence for the mean correlation time, $\langle \tau_c \rangle = \tau_0 \exp[D/(T - T_0)]$, as expected for spin-glass dynamics. The blue solid line corresponds to the model based on Kitaev fractional excitations.

While the experimental $1/T_1$ data at both fields nearly coincide, the BPP/Vogel-Fulcher prediction at 4.7 T shifts markedly to lower temperatures, reflecting the expected field dependence for conventional spin-glass freezing through the NMR Larmor frequency at $\omega_L \langle \tau_c \rangle \sim 1$. The inability to reproduce the observed overlap of the experimental $1/T_1$ data, demonstrates that the relaxation dynamics cannot be explained by a conventional spin-glass freezing mechanism. More details are given in Supplementary Note 5.

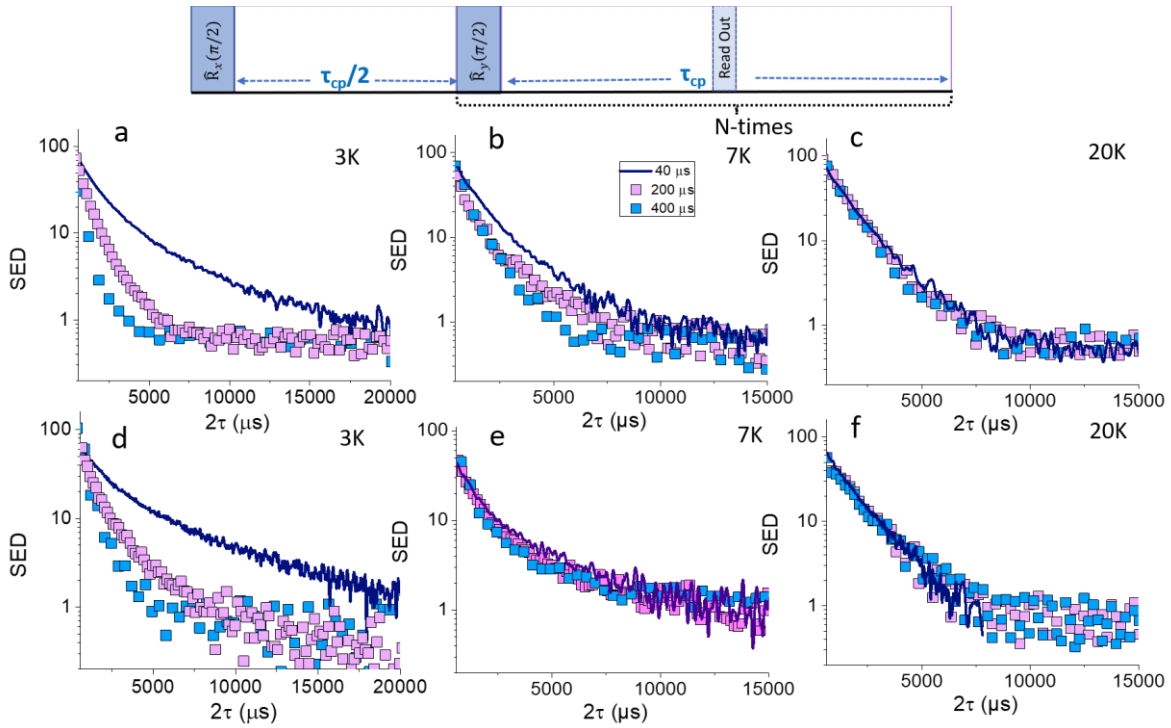

Supplementary Figure S6 | ^{23}Na NMR Spin Echo Decay (SED) signal intensity obtained by implementing a q-CPMG pulse sequence for various τ_{cp} values (40, 200 and 400 µs). a-c, the SEDs in magnetic field of 9.4 T at (a) 3K, (b) 7K and (c) 20K. **d-f,** the SEDs in magnetic field of 4.7 T at (d) 3K, (e) 7K and (f) 20K.

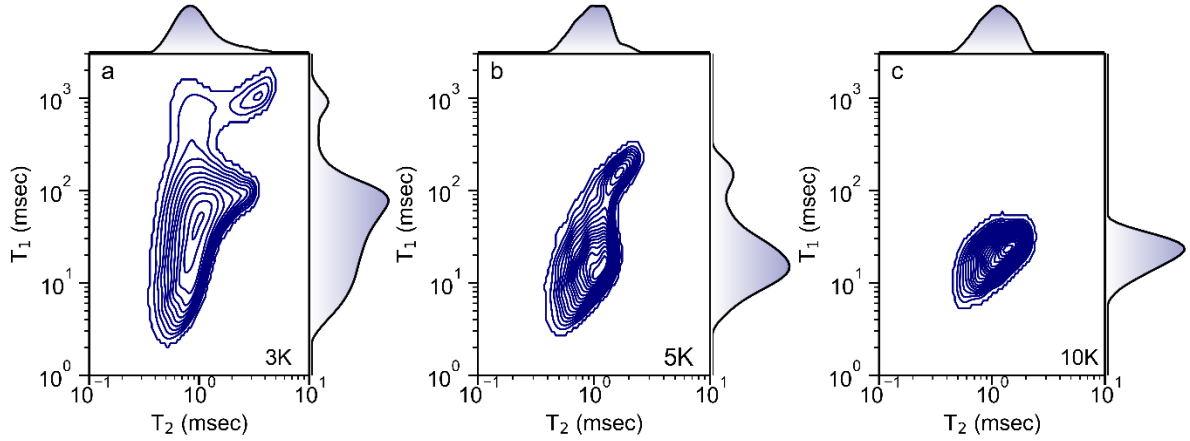

Supplementary Figure S7 | ^{23}Na NMR T_1-T_2 correlation spectroscopy spectra in magnetic field 9.4 Tesla. By increasing temperature, the long T_1 / T_2 component that is clearly seen at 3K gradually diminishes and disappears at temperatures above 10 K. Simultaneously, the short component of the T_1 distribution becomes narrower.

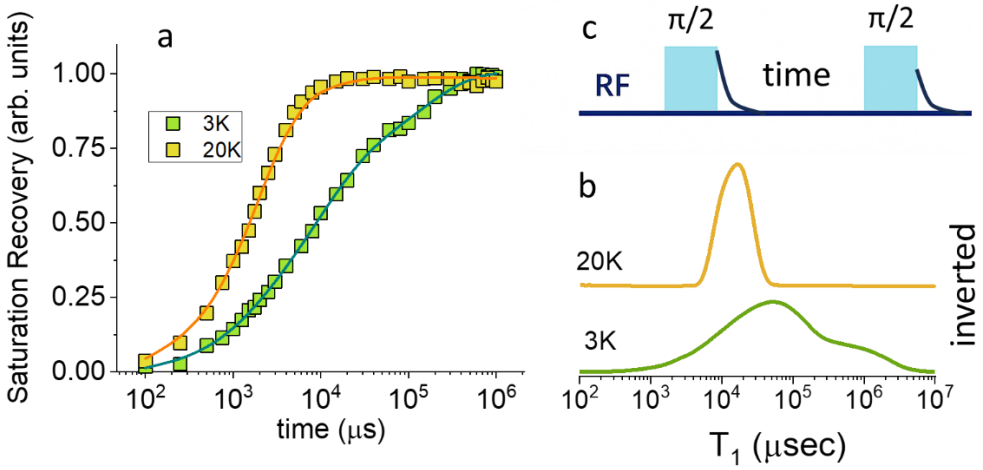

Supplementary Figure S8 | ^{23}Na NMR T_1 experiments of NCTO at 9.4 Tesla. a, Saturation recovery curves measured at 3K and 20K. **b,** Corresponding T_1 distributions derived by inverting the saturation recovery curves. **c,** Schematic representation of the saturation recovery pulse sequence. Signal measurements are obtained following the second pulse as a function of the interpulse interval.

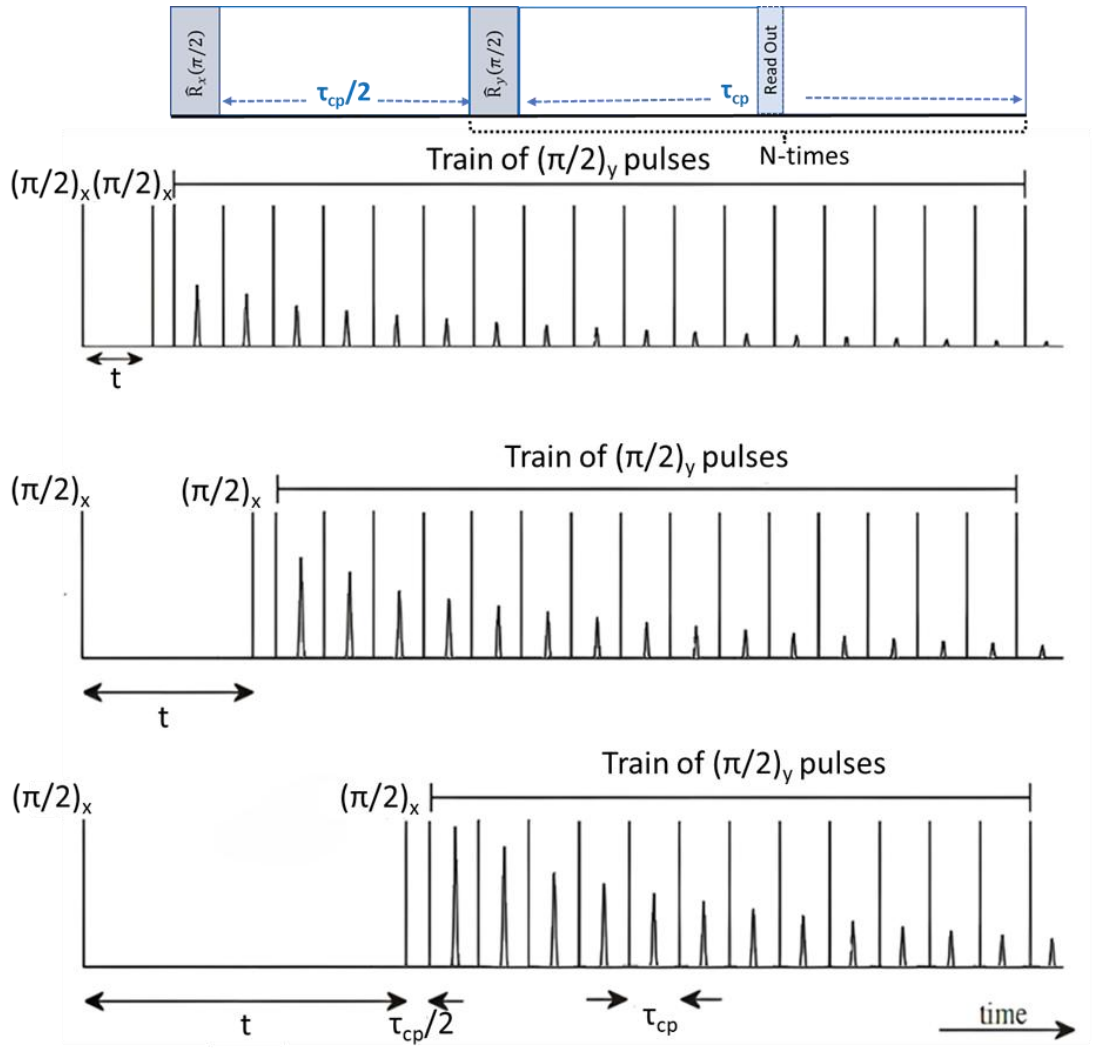

Supplementary Figure S9 | The $T_1 - T_2$ correlation spectroscopy pulse sequence. Three distinct instants of the saturation recovery variant of the $T_1 - T_2$ pulse sequence. The upper panel shows the quadrupolar Carr-Purcell-Meiboom-Gill (q-CPMG) part of the pulse sequence.

Atom	Wyckoff position	x	y	Z	Occ.
O	12i	0.0306	0.344	0.6727	1
Co(1)	2b	0	0	¼	1
Co(2)	2d	2/3	1/3	¼	1
Te	2c	1/3	2/3	¼	1
Na(1)	6g	0.38	0.38	½	0.57
Na(2)	2a	0	0	0	0.29
$\chi^2 = 0.808$					

Supplementary Table S1: Refined structural parameters of $Na_2Co_2TeO_6$ in the space group *P6₃22* (No. 182), obtained from powder XRD data at RT, with Na occupying two inequivalent crystallographic

positions, denoted as Na(1) and Na(2). The unit cell parameters are a = b = 5.2744 (Å), c = 11.2387 (Å), volume = 270.7695 Å^3.

Supplementary Notes

Supplementary Note 1: X-ray diffraction (XRD) was utilized to determine the crystallographic structure of the $Na_2Co_2TeO_6$ compound. The XRD spectra were recorded with an analytical PANalytical X'Pert PRO powder diffractometer. The sample was mounted on a zero-background holder and scanned by using Cu-Kα radiation (λ = 1.5418 Å) with the following experimental conditions: applied voltage of 40 kV, intensity of 30 mA, angular range (2θ) 5–90° and 0.03 steps/s. Rietveld refinement of obtained powder XRD pattern was carried out using the FULLPROF program software[1,2].

Figure S1a presents the X-ray diffraction (XRD) powder pattern of $Na_2Co_2TeO_6$ collected at 296 K, accompanied by refinement data, including calculated and background difference profiles. The results verify the compound's purity, and all diffraction peaks are indexed to a hexagonal cell with space group *P6₃22* (No. 182). The unit cell parameters are a = b = 5.2744 Å, c = 11.2387 Å. The most prominent peak corresponds to the (002) plane, further confirming the formation of the hexagonal crystal structure[3-5]. The (002), (101), (102), (004), (110), (112), (104), (114), and (300) lattice planes were found to have 2θ of 15.76°, 20.98°, 25.10°, 31.82°, 33.97°, 37.646°, 37.648°, 47.23°, and 60.78°, respectively, values consistent with those found in the literature[3-5]. Further structure analysis showed that the Na ions can partially occupy nonequivalent crystallographic positions in different percentages: 57% of the Na reside on sites of symmetry with Wyckoff position index 6g and 29% are in positions with site symmetry 2a (Table S1).

Panel (b) of Fig. S1 displays a comparison between the XRD pattern obtained from the relaxed 2x2x2 NCTO supercell using VESTA crystal analysis software and the experimental Rietveld analysis shown in Fig. S1a. The results demonstrate a strong correspondence between the two patterns, supporting the suitability of the NCTO supercell as a representative model of the actual material.

Supplementary Note 2:

A Python-based fitting routine was developed to deconvolute overlapping MAS sideband patterns in ^{23}Na NMR spectra of NCTO by simultaneously fitting pseudocontact shift (PCS) tensor parameters for two distinct sodium sites. The procedure combines Monte Carlo sampling of site-specific parameter distributions with full powder-averaging over a fixed orientation grid and uses the Covariance Matrix Adaptation Evolution Strategy (CMA-ES) for robust global optimization in a high-dimensional parameter space[6,7].

In the point-dipole PCS model, the through-space dipolar field from a paramagnetic center at distance r produces an NMR frequency shift[8]

$$\delta_{PCS}(\theta,\phi) = \frac{1}{12\pi r^3}[\chi_{ax}(3\cos^2\theta - 1) + 3\chi_{rh}\sin^2\theta\, cos2\phi], \text{ (S1)}$$

where χ_{ax} is the axiality, and χ_{rh} the rhombicity of the susceptibility tensor, and (θ, ϕ) the polar angles of r in the principal-axis frame of reference. Distances r are drawn from truncated Gaussian distributions defined by their mean and standard deviation. The isotropic shift δ_{iso} for each site, which includes chemical shift, contact shift, and bulk susceptibility contributions, was treated as an independent Gaussian-distributed parameter. Second-order quadrupolar effects on the ^{23}Na central transition were included as static orientation-dependent offsets for the isotropic position.

For MAS at frequency ω_r, the PCS anisotropy modulates the spinning sideband intensities via the Herzfeld–Berger Bessel formalism[9,10]. The modulation depth for sideband order k is

$$\beta(\theta, \phi) = \frac{2\pi\nu_0}{\omega_r}\delta_{PCS}(\theta, \phi), \text{ (S2)}$$

with ν_0 the ^{23}Na Larmor frequency. Sideband intensities are computed as

$$I_k = \left\langle J_k^2\left(\beta(\theta, \phi)\right)\right\rangle_{powder} e^{-\alpha|k|}, \text{ (S3)}$$

where J_k is the Bessel function of the first kind, the angular brackets denote averaging over the orientation grid, and $e^{-\alpha|k|}$ is an empirical order-dependent damping factor accounting for relaxation and other attenuation mechanisms.

For each Monte Carlo step of the site parameters, the orientation-averaged sideband manifold is generated and broadened with Lorentzian lineshapes. The two Na site-specific spectra are then scaled by their fitted populations and summed to produce the total simulated spectrum and subsequently compared to the experimental data in the CMA-ES optimization. The final fit yields the best-fit parameters, their distributions, and the individual site contributions.

Supplementary Note 3:

Bond-Length Dependence of Kitaev Superexchange

The strong bond-length dependence of the Kitaev exchange constant in edge-sharing cobaltates arises from the microscopic mechanism of ligand-mediated superexchange. For π-type overlaps between Co d orbitals and O p orbitals, the hopping integral can be approximated within Harrison's tight-binding framework as, $V_{pd\pi}(r) \propto r^{-2.5}$, where r is the metal-oxygen distance[11]. In the two-step process $\mathrm{Co} \rightarrow \mathrm{O} \rightarrow \mathrm{Co}$, the effective metal-metal hopping amplitude is then $t_{\mathrm{eff}}(r) \sim \frac{V_{pd\pi}(r)^2}{\Delta_{pd}} \propto r^{-5}$, with Δ_{pd} the charge-transfer energy[11]. Since the Kitaev superexchange constant scales as, $K(r) \sim \frac{t_{\mathrm{eff}}(r)^2}{U_{\mathrm{eff}}} \propto r^{-10}$, where U_{eff} is the effective on-site Coulomb repulsion[12,13], the resulting exponent reflects the fourth-power dependence on the underlying metal-ligand overlap.

Goodenough's orbital symmetry rules emphasize that for near-90° M-O-M bonds, π-type overlaps dominate, and the anisotropy of the exchange is maximized[14]. Furthermore, modern tight-binding calculations on transition-metal oxides confirm that π-type hopping exponents typically lie in the range 5-10[15,16], which when squared yield effective superexchange exponents of 10-20. Within this

framework, adopting $p = 10$ for NCTO is physically justified. The implications of this steep scaling are significant: a small fractional change in bond length produces a magnified fractional change in the exchange constant, $\frac{\delta K}{K} \approx -10\frac{\delta r}{r}$.

Thus, a spread of ±3% in r translates into approximately ±30% variation in K. The steep radial factor r^{-10} therefore combines with the symmetry-controlled angular sensitivity encoded in the term $[1 - c(\theta - \theta_0)^2]$, yielding the full dependence of K on both Co-O bond lengths and Co-O-Co bond angles.

Supplementary Note 4:

Monte Carlo simulation of ^{23}Na NMR spectra:

The ^{23}Na static NMR lineshapes at 3 K were simulated with a custom Python routine applied to the DFT-relaxed 2×2×2 NCTO supercell. For the three spin configurations considered, the zigzag AFM, triple-q AFM, and the QSL-inspired state, the same NMR model was used, with only the Co-spin texture being varied.

First, the crystallographic structure was read from the relaxed 2×2×2 supercell, and all Co, Na(1)/Na(2), Te, and O positions were retained explicitly. For each Na-bearing site, the local electric-field gradient was estimated within a point-charge model by summing the contribution of neighboring formal charges over periodic images within a finite real-space cutoff, thereby contributing only a small secondary quadrupolar term. In parallel, the Co-Na dipolar couplings were precomputed by identifying, for each Na(1)/Na(2) position and each Co site, the shortest periodic Co-Na separation vector within the same cutoff. These quantities were then used to evaluate the orientation-dependent NMR shift for 10,000 Monte Carlo-sampled powder orientations of the external magnetic field. The dipolar shift, which mainly defines the NMR powder pattern, was calculated (in ppm) as

$\delta_{\mathrm{dip}} = \sum_j c_{d,j}\left[3(\mathbf{m}_j\cdot\hat{\mathbf{r}}_j)(\mathbf{u}\cdot\hat{\mathbf{r}}_j) - \mathbf{m}_j\cdot\mathbf{u}\right]$, with $c_{d,j} = \frac{\mu_0}{4\pi}\frac{\mu_e}{r_j^3 B_0} \times 10^6$, $\mathbf{u}$ is the random field orientation, and $\mathbf{m}_j = (s_x, s_y, s_z)$ is the dimensionless spin direction.

The resulting NMR shifts were subsequently summed to a Gaussian-smoothed simulated powder spectrum.

The distinction between the three simulated magnetic states lies entirely in the construction of the Co-spin pattern.

- For the zigzag AFM state, the Co moments were assigned layer by layer in a fixed collinear zigzag arrangement, and the resulting static texture was kept unchanged throughout the powder averaging.
- For the triple-q AFM state, the moments were constrained to follow one of the in-plane Co-Co bond directions, with additional rules enforcing a symmetry-consistent non-collinear pattern, imitating the triple-q spin structure; once generated, this texture was likewise kept fixed during the powder averaging.

- In the QSL-inspired simulation, we followed a different procedure. We first identified the in-plane Co-Co bonds in each honeycomb layer and then generated random nearest-neighbor spin-dimers covering each cobalt layer of the 2×2×2 supercell. For every selected Co-Co pair, the two spins were taken to be parallel to each other and confined to the ab plane, with their common direction chosen perpendicular to the corresponding bond, consistent with the local bond-selective character expected for Kitaev-type correlations. For each of the 10,000 random orientations of the external magnetic field, the spin-dimer covering of each layer in each crystallite was generated independently and randomly, so that every crystallite orientation was associated with a distinct spin-dimer configuration.

To mimic experimental signal averaging, the QSL NMR spectrum was not obtained from a single powder pattern. Since a QSL state consists of the superposition of independent realizations of the layer-resolved spin-dimer configurations for all crystallite orientations, the QSL lineshape was obtained by averaging over 40 powder patterns, each probing a different instantaneous local dimer configuration, rather than a unique static ordered state. This is the essential difference between the QSL simulation and the zigzag or triple-q AFM calculations: the latter probe a fixed static spin texture during NMR signal averaging, whereas the QSL case samples and averages an ensemble of many nearly degenerate, correlated spin configurations.

Supplementary Note 5:

Supplementary Figure S5b compares the measured ^{23}Na spin-lattice relaxation rate, $1/T_1$, at 4.7 T and 9.4 T with a Bloembergen-Purcell-Pound (BPP)-based model for thermally slowed local magnetic fluctuations. In the simplest BPP picture[17], the local hyperfine field at the nucleus is assumed to fluctuate with an exponentially decaying autocorrelation function characterized by an effective correlation time, τ_c. For an isotropic fluctuating local field then, the corresponding longitudinal NMR relaxation rate $1/T_1$ can be written as[17,18]

$$1/T_1 = \gamma_n^2 \langle h_\perp^2 \rangle [\tau_c/(1 + \omega_L^2 {\tau_c}^2) + 4\tau_c/(1 + 4\omega_L^2 {\tau_c}^2)] \text{ . (S4)}$$

Here, γ_n is the nuclear gyromagnetic ratio, $\langle h_\perp^2 \rangle = \langle h_x^2 \rangle + \langle h_y^2 \rangle$ is the mean-square transverse fluctuating local field at the nucleus, and $\omega_L = \gamma_n B_0$ is the NMR Larmor frequency in magnetic field B_0. In this framework, the maximum in $1/T_1(T)$ is expected when $\omega_L \tau_c \sim 1$; therefore, reducing the magnetic field should shift the characteristic relaxation maximum to lower temperature once the fluctuations slow down on cooling.

To represent a conventional glassy slowing-down scenario, which is characterized by a broad distribution of correlation times, we used a Vogel-Fulcher form[19] for the mean correlation time,

$$\langle \tau_c \rangle = \tau_0 \, exp[D/(T - T_0)] \text{ . (S5)}$$

In Eq. (S5), τ_0 is a microscopic attempt time, D controls the strength of the slowing down, and T_0 is the Vogel-Fulcher temperature at which the representative timescale would formally diverge. This

parametrization provides a conventional benchmark for the temperature evolution of the relaxation maximum in $1/T_1(T)$.

In this context, a set of BPP/Vogel-Fulcher parameters was chosen to provide the closest qualitative description of the 9.4 T $1/T_1$ data, as shown in Supplementary Figure S5. Subsequently, the corresponding 4.7 T curve was calculated by changing only the Larmor frequency ω_L. Within the adopted conventional spin-glass-freezing scenario this produces a field-induced displacement of the relaxation maximum, whilst the experimental ^{23}Na $1/T_1(T)$ data in both magnetic fields remain unchanged. The failure of the BPP model to simulate the experimental data shows that the T_1 relaxation mechanism cannot be accounted to conventional spin-glass freezing, but it is more naturally consistent with the Kitaev fractional-excitation mechanism discussed in the main text.

Supplementary Note 6:

In order to acquire the ^{23}Na NMR spin-spin relaxation time T_2 distribution function $g(T_2)$, the experimental spin-echo decay curves were modelled with a Fredholm integral equation of the first kind[20,21], $\frac{M(t)}{M(0)} = \int_0^{+\infty} k_0(T_2,t)g(T_2)d(log_{10}T_2)$, (S6)

where $\frac{M(t)}{M(0)}$ is the normalized spin echo decay and $k_0(T_2,t) = exp\left(-\frac{t}{T_2}\right)$. This equation can be transformed in a vector matrix notation to $M = K_0 g$, which in turn can be inverted to obtain the $g(T_2)$ distribution function[20,21]. In the present work, the inversion was achieved by implementing a modified non-negative Tikhonov regularization algorithm[21].

The contour plot in Figures 4b and 4d of the main article are made of 50 $g(T_2)$ curves, acquired at 50 consecutive resonance frequencies, covering the whole ^{23}Na NMR spectra. Ultrasoft pulses ($90^o \sim 20$ μsec) were used so that each time a narrow frequency bandwidth was irradiated.

The spin-lattice relaxation time distribution function $g(T_1)$ was derived using a similar method as $g(T_2)$, by replacing the kernel $k_0(T_2,t)$ in the integral equation with $k_0(T_1,t) = 1 - 0.9exp\left(-\frac{6t}{T_1}\right) - 0.1exp\left(-\frac{t}{T_1}\right)$, (S7)

that is valid for transitions between the m =±1/2 states (central transition), in case of $I = 3/2$ nuclear spins (Refs. [18, 35] of the main article).

Finally, the T_1-T_2 correlation spectra were obtained by inverting a series of q-CPMG trains, after applying an initial 180^0 pulse at varying delays from the q-CPMG train, to encode in the t_1 direction the T_1, as shown in supplementary Figure S7. The series of q-CPMG spin-echo decays were modelled as $\frac{g(t_1,t_2)}{g(0,0)} = \iint_{-\infty}^{+\infty} k_0(T_1,t_1;T_2,t_2)g(T_1,T_2)d(log_{10}T_1)d(log_{10}T_2)$, (S8)

and subsequently inverted with a 2D Tikhonov regularization algorithm[20,21]. The kernel $k_0(T_1,t_1;T_2,t_2)$ in the 2D case is the cross product of the two previous kernels for the T_1 and T_2 inversions.

Supplementary Note 7:

The transverse quadrupolar relaxation time, T_{2q}, is typically measured using the two-pulse quadrupolar echo (QE) sequence, $90_x - \tau - 90_y - \tau$ [22]. However, this basic sequence is limited in its ability to probe slow fluctuations, particularly when the correlation time τ_c exceeds the motional narrowing limit ($\tau_c \gg \tau_M$). In such cases, the quadrupolar Carr-Purcell-Meiboom-Gill (q-CPMG) sequence provides a more suitable alternative[23]. This sequence, also known as the Mansfield-Ware (MW-4) pulse train[24], in its general form consists of $90_x - \frac{\tau_{cp}}{2} - (\phi_y - \tau_{cp})_N$, where τ_{cp} is the inter-pulse delay, ϕ denotes the spin-flip angle, and N the number of repetitions. The schematic of this sequence is shown on top of Supplementary Figure S6.

In paramagnetic systems such as NCTO, relaxation is dominated by interactions between nuclear spins (I) and fluctuating electron spins (S). Blicharski[25,26] demonstrated that the effective transverse dipolar relaxation rate, $1/T_{2q}$, arising from pseudo-contact relaxation due to electron-spin fluctuations, can be expressed as:

$$1/T_{2q} = \tau_c \langle S^2(0) \rangle \{1 - (\tau_c/\tau_{cp}) tanh(\tau_{cp}/\tau_c)\} \left\{ (1 - \cos\varphi) / \left(1 - \cos\varphi / cosh\left(\frac{\tau_{cp}}{\tau_c}\right) \right) \right\} \text{ (S9),}$$

This expression is derived under the approximation that the time-dependent hyperfine Hamiltonian can be written as $H_{hf}(t) = A_{SD}\, S(t)\, I_z$, with the electron-spin autocorrelation function modeled as an exponential decay, $\langle S(t)S(t-\tau) \rangle = \langle S^2(0) \rangle\, e^{-\tau/\tau_c}$. Following the derivation steps outlined in Supplementary Ref. [27], Eq. (S9) is obtained.

For the special case of a 90° flip angle ($\phi = 90°$), Eq. (S9) simplifies to:

$$1/T_{2q} = \tau_c \langle S^2(0) \rangle \{1 - (\tau_c/\tau_{cp}) tanh(\tau_{cp}/\tau_c)\} \text{ (S10)}$$

which corresponds to Eq. (3) in the main article.

Other relaxation pathways - quadrupolar relaxation via fluctuating electric field gradients and through-bond hyperfine (Fermi-contact) relaxation - yield formally similar expressions. However, in NCTO the dominant mechanism is dipolar relaxation driven by electron-spin fluctuations[28].

Supplementary References

1. Rodríguez-Carvajal, J. Recent advances in magnetic structure determination by neutron powder diffraction. *Physica B: Condensed Matter* **192**, 55–69 (1993).

2. Rodríguez-Carvajal, J. Recent Developments of the Program FULLPROF. *Newsletter in Commission on Powder Diffraction (IUCr)* **26**, 12–19 (2001).

3. Xiao, G. et al. Crystal Growth and the Magnetic Properties of $Na_2Co_2TeO_6$ with Quasi-Two-Dimensional Honeycomb Lattice. *Crystal Growth & Design* **19**, 2658–2662 (2019).

4. Berthelot, R., Schmidt, W., Sleight, A. W. & Subramanian, M. A. Studies on solid solutions based on layered honeycomb-ordered phases P2-$Na_2M_2TeO_6$ (M = Co, Ni, Zn). *J. Solid-State Chem.* **196**, 225–231 (2012).

5. Viciu, L. et al. Structure and basic magnetic properties of the honeycomb lattice compounds $Na_2Co_2TeO_6$ and $Na_3Co_2SbO_6$. *J. Solid-State Chem.* **180**, 1060–1067 (2007).

6. Hansen, N.; Ostermeier, A. Completely derandomized self-adaptation in evolution strategies. *Evol. Comput.* **9**, 159-195 (2001).

7. Press, W. H.; Teukolsky, S. A.; Vetterling, W. T.; Flannery, B. P. Numerical Recipes in C: The Art of Scientific Computing, 2nd ed.; Cambridge University Press: Cambridge, 1992.

8. Suturina, E. A., et al. Beyond Bleaney's Theory. Experimental and Theoretical Analysis of Periodic Trends in Lanthanide Induced Chemical Shift. *Angew. Chem. Int. Ed.* **56**, 12215–12218 (2017).

9. Herzfeld, J.; Berger, A. E. Sideband intensities in NMR spectra of samples spinning at the magic angle. *J. Chem. Phys.* **73**, 6021-6030 (1980).

10. Sun, B. Q.; Pines, A. An approximate method of sideband intensity calculation in magic angle spinning NMR. *Appl. Magn. Reson.* **5**, 43–61 (1993).

11. W. A. Harrison, *Electronic Structure and the Properties of Solids* (Freeman, 1980), Chs. 3-4, pp. 110–115; Tight-binding theory of molecules and solids, *Pure &App. Chem.* **61**, 2161-2169 (1989).

12. P. W. Anderson, "Antiferromagnetism. Theory of superexchange interaction," *Phys. Rev.* **79**, 350 (1950).

13. J. B. Goodenough, *Magnetism and the Chemical Bond* (Interscience, 1963), pp. 164-170.

14. J. B. Goodenough, ibid., orbital symmetry rules for 90° vs 180° superexchange.

15. J.-M. Jancu et al., "Empirical spds* tight-binding calculation for cubic semiconductors: General method and material parameters", *Phys. Rev. B* **57**, 6493 (1998).

16. T. B. Boykin et al., "Empirical tight-binding parameters for group IV and III-V semiconductors," *Phys. Rev. B* **66**, 125207 (2002).

17. Bloembergen, N., Purcell, E. M. & Pound, R. V. Relaxation effects in nuclear magnetic resonance absorption. *Phys. Rev.* **73**, 679–712 (1948).

18. Abragam, A. *The Principles of Nuclear Magnetism* (Oxford Univ. Press, 1961).

19. Bag, P., Baral, P. R. & Nath, R. Cluster spin-glass behavior and memory effect in $Cr_{0.5}Fe_{0.5}Ga$. *Phys. Rev. B* **98**, 144436 (2018).

20. Mitchell, J., Chandrasekera, T. C. & Gladden, L. F. Numerical estimation of relaxation and diffusion distributions in two dimensions. *Prog. Nucl. Magn. Reson. Spectrosc.* **62**, 34-50 (2012).

21. Day, I. J. On the inversion of diffusion NMR data: Tikhonov regularization and optimal choice of the regularization parameter. *J. Magn. Reson.* **211**, 178–185 (2011).

22. Davis, J. H., Jeffery, K. R., Bloom, M., Valic, M. I. & Higgs, T. P. Quadrupolar echo deuteron magnetic resonance spectroscopy in ordered hydrocarbon chains. *Chem. Phys. Lett.* **42**, 390–394 (1976).

23. Bloom, M. & Sternin, E. Transverse Nuclear Spin Relaxation in Phospholipid Bilayer Membranes. *Biochemistry* **26**, 2101–2105 (1987).

24. Mehring, M. *Principles of High-Resolution NMR in Solids*. Springer-Verlag, Berlin (1983).

25. Blicharski, S. Nuclear-spin relaxation in the presence of Mansfield-Ware-4 multipulse sequence. *Can. J. Phys.* **64**, 733–735 (1986).

26. Blicharski, S. & Wolak, A. Nuclear Spin Relaxation in periodically perturbed systems. II Like and unlike spins. *Acta Phys. Pol. A* **82**, 511–515 (1992).

27. Lankhorst, D., Schriever, J. & Leyte, J. C. The Time Evolution of the Transverse Magnetization in Carr-Purcell Sequences in the Presence of Chemical Exchange. *J. Magn. Reson.* **51**, 430–437 (1983).

28. Kikuchi, J. et al. Field evolution of magnetic phases and spin dynamics in the honeycomb lattice magnet $Na_2Co_2TeO_6$: ^{23}Na NMR study. *Phys. Rev. B* **106**, 224416 (2022).